Heliyon 10 (2024) e25832

Contents lists available at ScienceDirect

Heliyon

journal homepage: www.cell.com/heliyon

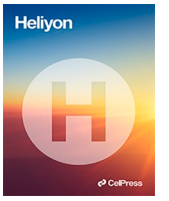

Research article

# Fabrication and properties of hydroxyapatite/chitosan composite scaffolds loaded with periostin for bone regeneration

Huachun Wang [a,b], Ruixue Sun [c], Shengyun Huang [d], Haiwei Wu [d], Dongsheng Zhang [a,d,*]

[a] *Department of Oral and Maxillofacial Surgery, School and Hospital of Stomatology, Cheeloo College of Medicine, Shandong University & Shandong Key Laboratory of Oral Tissue Regeneration & Shandong Engineering Laboratory for Dental Materials and Oral Tissue Regeneration, Jinan, 250012, China*

[b] *Department of Oral and Maxillofacial Surgery, Qilu Hospital of Shandong University, Qingdao, 266035, China*

[c] *College of Materials Science and Engineering, Qingdao University of Science and Technology, Qingdao, 266042, China*

[d] *Department of Stomatology, Shandong Provincial Hospital Affiliated to Shandong First Medical University, Jinan, 250012, China*

ARTICLE INFO

*Keywords:*
Chitosan
Hydroxyapatite
Periostin
Composite scaffold
Bone regeneration

ABSTRACT

This paper reports a facile fabrication method of hydroxyapatite/chitosan (HAp/CS) composite scaffold with 3D porous structure without using any chemical cross-linkers. The HAp particles had an urchin-like hollow microstructure and high surface area, which was uniformly dispersed into the pore walls of the HAp/CS scaffold. The addition of HAp can efficiently enhance the mechanical properties and bioactivity of the HAp/CS scaffold. Moreover, periostin was successfully loaded onto the HAp/CS scaffold. When applied to the repair of bone defect in a rat mandibular model, the HAp/CS scaffold loaded with periostin can enhance osteointegration and accelerate bone regeneration. Our research combines periostin with the HAp/CS composite material, which provides a novel strategy to improve bone regeneration and has great application prospect in bone repair fields.

## 1. Introduction

Most of the common bone defects in oral and maxillofacial region are caused by trauma, inflammation or tumor. Although bone tissue has good self-healing ability, large area of bone defects cannot regenerate via normal physiological processes [1,2]. Alveolar bone resorption after edentulous is also a common problem in clinical practice, which causes different degrees of difficulty in implant denture repair. In order to create favorable conditions for implant denture repair, bone substitutes for bone filling and repair are often used in bone augmentation surgery. Although, to date, autologous and allogenous bone grafts are still the main forms in clinical therapy, they possess the drawbacks of limited availability and the risk of donor site morbidity and disease transmission [3–5]. Thus, artificial bone replacement materials have attracted considerable attention for promoting bone regeneration. An ideal artificial bone should have a three-dimensional porous structure, good biocompatibility, adaptable degradation rate, adequate mechanical properties and so on [6–8].

* Corresponding author.Department of Oral and Maxillofacial Surgery, School and Hospital of Stomatology, Cheeloo College of Medicine, Shandong University & Shandong Key Laboratory of Oral Tissue Regeneration & Shandong Engineering Laboratory for Dental Materials and Oral Tissue Regeneration, Jinan, 250012, China.

*E-mail address:* ds63zhang@sdu.edu.cn (D. Zhang).

https://doi.org/10.1016/j.heliyon.2024.e25832
Received 20 November 2023; Received in revised form 30 January 2024; Accepted 2 February 2024
Available online 17 February 2024

Chitosan (CS) is a promising biomaterial and has been widely used in wound healing, drug delivery and tissue engineering due to its outstanding bioactivity, biodegradability, antibacterial activity and biocompatibility [9,10]. However, pure CS usually has a weak mechanical property and exhibits poor cell adhesion [11]. In order to overcome these problems, CS is often combined with other polymers or bioceramics [12–14]. Hydroxyapatite ($Ca_{10}(PO_4)_6(OH)_2$, HAp) is the main inorganic component of human bones and teeth. Due to its excellent biocompatibility, osteoconductivity and bioactivity, HAp has been widely studied and used in bone repair and bone tissue engineering fields [15–18]. Nevertheless, HAp has some limitations such as insufficient mechanical properties, low plasticity and low biodegradability. Therefore, HAp is often combined with other biopolymers such as alginate, collagen, and PLA to obtain composite materials with optimized properties to meet the quality and functionality requirements for a bone substitute [19,20]. The incorporation of CS with HAp can combine the inherent advantages of both CS and HAp and overcome their respective limitations [13,21].

Recently, various methods have been used to fabricate HAp/CS composite scaffolds, such as freeze-drying [22], in situ precipitation [23], coacervation technique [24] and electrospinning [25]. In these methods, cross-linking treatment through using crosslinkers such as glutaraldehyde and glyoxal was often used to increase the mechanical properties and chemical stability of HAp/CS scaffold [26]. However, these crosslinkers have physiological toxicity and can affect the biosafety and biocompatibility of the scaffold. On the other hand, the morphology, microstructure and surface area of the used HAp particles also have important effects on the properties of the HAp/CS scaffold. HAp nanoparticles, nanowires and nanofibers were frequently used in the preparation of the HAp/CS composite scaffolds [27–29].

Periostin is an extracellular matrix protein, which can bind to stem cells and play an important role in inflammatory responses and tissue repair [30]. It has been reported that periostin can regulate the osteogenic activity and process of osteoblasts. Maintaining a certain level of periostin not only accelerates bone formation, but also results in high bone quality and shortened bone formation time, which helps to achieve bone repair in bone defect areas earlier. Cai et al. reported that periostin is closely related to the genes Runx2 and RANKL involved in bone remodeling. Low expression of periostin can lead to low expression of Runx2, which delays fracture healing, suggesting that periostin can promote fracture healing [31]. However, there have been no reports on loading periostin onto bone repair scaffolds to be used as bone filling and repair materials.

In this study, the HAp/CS composite scaffolds were firstly fabricated through using a facile freeze-drying process. No cross-linking agent was used during the preparation. The effects of the addition of HAp hollow microspheres on the structure, porosity, swelling ratio and mechanical properties of the HAp/CS scaffolds were thoroughly studied. Moreover, periostin was loaded onto the HAp/CS scaffold and was applied to a rat mandibular defect model for in vivo experiments to evaluate the bone repair effect and to explore the role of periostin in the bone healing process. The HAp/CS composite scaffold loaded with periostin has shown great potential application in the field of bone repair.

## 2. Materials and methods

### 2.1. Materials

Calcium nitrate tetrahydrate [$Ca(NO_3)_2{\cdot}4H_2O$], diammonium phosphate [$(NH_4)_2HPO_4$], sodium hydroxide (NaOH), Chitosan (80–95% deacetylated), acetic acid and all the inorganic salts for PBS were purchased from China Pharmaceutical Group Chemical Reagents Co., Ltd (China). Polyaspartic acid (PASP) was obtained from Chengdu Gracia Chemical Technology Co., Ltd (China). All chemicals were used without further purification. Deionized (DI) water was used in all the experiment.

### 2.2. Fabrication of HAp/CS composite scaffolds

The HAp hollow microspheres were firstly synthesized as described in our previous studies [32,33]. Cylindrical HAp/CS composite scaffolds were fabricated via a simple vacuum freeze-drying method. Firstly, the CS solution was prepared by dissolving 2.0 g CS powder in 50 mL acetic acid (2 vt. %) and stirred for 6 h. Then, a specific amount of HAp powder was added into the CS solution and was kept under stirring for 1 h at room temperature. The mixed solution was filled into each well of 24-well plates, frozen at −18 °C for 24 h. Afterwards, the frozen mixtures were removed from the 24-well plates and freeze-dried at −50 °C for 72 h. The resulting scaffolds were neutralized through immersing in a 10 wt% NaOH solution for 12 h to remove the excess acetic acid and washed with deionized water. Finally, the above wet scaffolds were freeze-dried again to obtain the final dry scaffolds. According to the ratio of HAp mass to the volume of CS solution, the prepared scaffolds are marked as 1%, 2%, 3% and 4% HAp/CS, respectively.

### 2.3. Characterization

The microstructure and morphology of the samples were characterized by field emission scanning electron microscope (FESEM, JEOL JSM-6700F) and transmission electron microscopy (TEM, JEOL JEM-2100). The phase composition of the samples was characterized by X-ray diffraction (XRD, Rigaku, D/max-2500/PC) with Cu Kα radiation. The FTIR spectra were recorded by a Fourier transform infrared spectrometer (FTIR, Bruker, Tensor 27) in the range of 4000–400 $cm^{-1}$ with a resolution of 4.0 $cm^{-1}$.

### 2.4. Porosity measurement

The porosity of different HAp/CS scaffolds was measured according to the Archimedes method. The mass of the flask filled with

anhydrous ethanol (to tick mark) was a weight of $W_1$, the mass of the dry scaffold was $W_s$. After the scaffold fully saturated with anhydrous ethanol being putted into the flask, the anhydrous ethanol spilling the tick mark was sucked and discarded and then weighted ($W_2$). The mass of the flask after removing the scaffold was $W_3$. The porosity of scaffolds was determined using Eq. (1) [34,35]:

$$\text{Porosity}\ (\%) = (W_2 - W_3 - W_s) / (W_1 - W_3) \times 100\% \quad (1)$$

### 2.5. Swelling testing

To measure the swelling ratio of the scaffolds, lyophilized scaffolds were weighed ($W_d$) and soaked in phosphate buffer saline solution (PBS) (pH = 7.4) at 37 °C for 24, 48 and 72 h. Swollen scaffolds were weighed ($W_s$) after excess solution remaining on their surface was absorbed with a filter paper. The swelling ratio of the scaffolds was calculated according to the following Eq. (2) [36,37]:

$$\text{Swelling raio}\ (\%) = (W_s - W_d) / W_d \times 100\% \quad (2)$$

### 2.6. Mechanical testing

Prior to the compressive testing, the scaffolds (Φ10 × 10 mm) were soaked in PBS solution (pH = 7.4) at 37 °C for 24 h [13,38]. Compressive testing was performed on a dynamic mechanical analyzer (DMA, Q800) at a displacement rate of 0.05 mm $s^{-1}$. The compressive elastic modulus was calculated as the slope of the initial linear portion of the stress-strain curve.

### 2.7. In vitro cell experiments

#### 2.7.1. Cell adhesion and growth

Mouse osteoblast-like MC3T3-E1 cells (Shanghai Institutes for Biological Sciences, Chinese Academy of Sciences) were used for in vitro cell study. The scaffolds were cut into disk-like samples with 10 mm in diameter and 2 mm in thickness, which was exposed to UV radiation for disinfection on both sides for 30 min. Theses samples were placed in 24-well plates and seeded with cell suspension at a density of $3 \times 10^5$ cells $mL^{-1}$. The cell culture conducted at 37 °C in a humidified incubator with 5% $CO_2$ and 95% air. The culture medium was changed every 2 days. After 12 days of culturing, the samples were removed from the medium and gently washed with PBS. Then, the cells on the samples were immobilized with 3% glutaraldehyde for 2 h at 4 °C. They were subsequently dehydrated for 15 min with each ethanol series (30%, 50%, 70%, 80%, 90%, 95%, and 100%). Finally, they were freeze-dried, sputtered with gold and examined with a FESEM for observation of cell adhesion and morphologies.

#### 2.7.2. Alkaline phosphatase activity

The alkaline phosphatase (ALP) activity of MC3T3-E1 cells was estimated by using the ALP assay kit (Biyuntian, China). Briefly, scaffolds were placed in 24-well plate and MC3T3-E1 cell suspension at a density of $3 \times 10^5$ cells $mL^{-1}$ was seeded onto each scaffolds and then cultured with osteogenesis induction medium at 37 °C for 3, 7, and 14 days. At each time point, cells were lysed by Western and immunol precipitation (IP) without inhibitors (Biyuntian, China), protein concentration were assayed by BCA Protein Concentration Assay Kit (Boster, China). The concentration of protein of each sample was diluted to the same for the relative quantitative measurements of ALP according to manufacturer's instruction. The absorbance at 405 nm was measured with a microplate reader.

### 2.8. In vivo experiments

#### 2.8.1. Rat mandibular defect model

Eighteen Wistar rats aged 8 weeks, were used to establish a rat mandibular defect model in this study. The Wistar rats were firstly randomly divided into 4 groups: control group with empty bone defect; CS group; 3%HAp/CS group; 3%HAp/CS group loaded with periostin (3%HAp/CS + Periostin). After exposure of mandible, a defect with the size of 5 mm × 4 mm × 1 mm was created. The scaffolds were cut into the same size and implanted into the mandibular bone defect area. The defect was left empty in the control group. Then the wounds were sutured carefully. At 2 weeks, 4 weeks, and 8 weeks after surgery, the rats were sacrificed and the mandibles with implantations were harvested and fixed in 4% paraformaldehyde solution for further analysis.

#### 2.8.2. Micro-CT evaluation

The bone samples were examined by Micro-CT (μCT 100, Scanco Medical, Switzerland) at a voltage of 70 kvp and an electric current of 200 μA. The 3D images of the defects were reconstructed using the MIMICS software package (Materialise, US). The ratio of bone volume/tissue volume (BV/TV) was calculated through using analysis software.

#### 2.8.3. Histological analysis

For H&E and Masson's trichrome staining, the samples were fixed in 4% formalin for 24 h, dehydrated with a graded series of ethanol and embedded in paraffin. Then, the samples were cut to a thickness of 5 μm, which was stained with Hematoxylin- Eosin and Masson's Trichrome Stain Kit according to manufacturer's protocol, and observed with optical microscope.

#### 2.8.4. Immunohistochemical analysis

The surface wax was removed from the paraffin slices through washing with xylene solution twice for 10 min each time. Afterwards, the samples were hydrated with 100% I, 100% II, 90%, 85%, and 70% gradient alcohol in sequence for 2 min each time and rinsed with double distilled water. Then, the samples were soaked in 3% hydrogen peroxide for 30 min and rinsed with PBS. At room temperature, the slices were wet packing treatment in 1% BSA-PBS for 20 min, then the primary antibody diluent was added and stayed overnight at 4 °C. On the second day, the slices were placed back at room temperature for 1 h and rinsed with PBS. The secondary antibody diluent was added and incubated for 1 h before rinsing with PBS. The DBA coloring solution was dropped onto the tissue, the color development was observed by a microscope and terminated in a timely manner. The slices were stained with 1% methyl green for 15 min and rinsed with PBS, and then hydrated with 100% I, 100% II, 90%, 85%, and 70% gradient alcohol in sequence. Finally, the slices were transparently treated twice for 2 min each time, and sealed with neutral gum. The staining results were evaluated by an optical microscope. All the staining positive areas (optical density, OD) were analyzed through using Image Pro Plus 6.0 (IPP 6.0) (Media Cybernetics, Silver Spring, MD).

#### 2.8.5. TRAP staining

The surface wax was removed from the paraffin slices through washing with xylene solution twice for 10 min each time. Afterwards, the samples were hydrated with 100% I, 100% II, 90%, 85%, and 70% gradient alcohol in sequence for 2 min each time and rinsed with double distilled water. The TRAP staining solution was added and stayed for 15 min at room temperature. After the red staining, the slices were washed with double distilled water three times. The slices were stained by methyl green for 10 min, followed by washing twice with double distilled water. Finally, the slices were sealed with glycerol aqueous. The staining results were evaluated by an optical microscope. All the staining positive areas (optical density, OD) were analyzed through using Image Pro Plus 6.0 (IPP 6.0) (Media Cybernetics, Silver Spring, MD).

### 2.9. Statistical analysis

The measured data were expressed as mean ± standard deviation. Statistical comparisons were performed by ANOVA for multiple comparisons, and the statistical significance was considered at $*p < 0.05$, $**p < 0.01$, and $***p < 0.001$.

## 3. Results and discussion

### 3.1. Morphology and microstructure of the scaffolds

The morphologies of the prepared HAp hollow microspheres are shown in Supplementary Fig. S1. It can be seen that the as-prepared HAp microsphere has a three-dimensional (3D) hierarchical microstructure assembled with many HAp nanoneedles. The average diameter of HAp microspheres is about 1 μm. Both FESEM and TEM images reveal that the microsphere has a hollow structure.

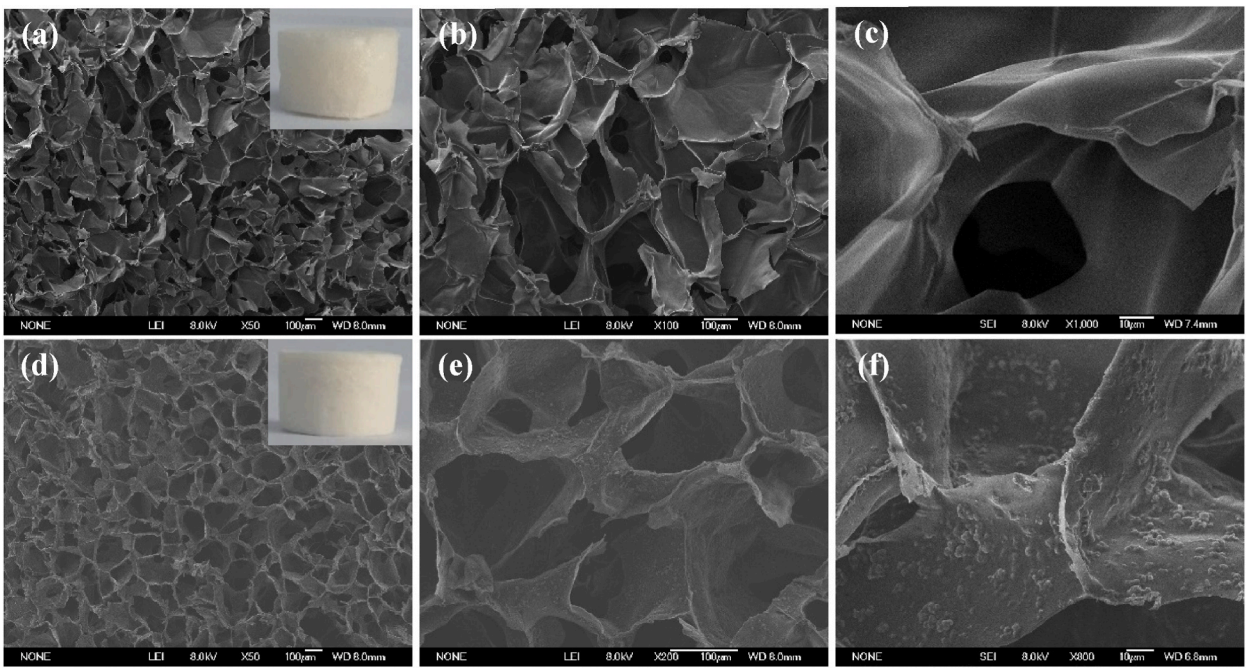


**Fig. 1.** FESEM images of (a–c) pure CS scaffolds and (d–f) 3% HAp/CS scaffolds.

Such a unique microstructure endows the HAp with a high specific surface area of 176 $m^2$ $g^{-1}$ and a hierarchical porosity.

Fig. 1 shows the FESEM images of transverse sections of pure CS and 3% HAp/CS scaffolds. The scaffolds are highly porous and exhibit a hierarchical structure with 3D interconnected open pores. On the whole, the addition of HAp microspheres does not decrease the porosity and pore size of CS matrix. The average diameter of the primary pores is about 100–200 μm, and the wall thickness of the pores is about 3–5 μm, which is favorable for nutrient transportation and cell infiltration and thus beneficial for new bone formation [22,39]. As shown in Fig. 1(a–c), the surface of pore walls of the pure CS scaffold is very clean and smooth. While the HAp/CS composite scaffold exhibits a rough pore surface (Fig. 1(d–f)). HAp microspheres are uniformly incorporated in the CS matrix, well-dispersed on the surface of pore walls without significant aggregate formation.

### 3.2. Phase composition of the scaffolds

XRD patterns of the HAp/CS composite scaffolds with different contents of HAp are shown in Fig. 2(a). It is observed that a very broad peak in XRD pattern of pure CS centered at about 21°, which is a characteristic amorphous phase peak of CS [22,40]. With the increase of HAp content, the intensity of this peak decreases gradually. The characteristic diffraction peaks for hexagonal HAp (JCPDS No. 09–0432) are clearly visible in both pure HAp and HAp/CS composite scaffolds. For the pure HAp, the intensity of all the peaks is low and broad, indicating a low crystallinity.

Fig. 2(b) shows the FTIR spectra of different samples. For pure HAp, the absorption bands at 602, 962, 1030, and 1097 $cm^{-1}$ are attributed to the $PO_4^{3-}$ stretching vibrations. The broad bands at 3429 $cm^{-1}$ are due to adsorbed water. The peaks at 1597 and 1420 $cm^{-1}$ are ascribed to $COO^-$ in PASP, which was added during the preparation of HAp hollow microspheres. For pure CS, the broad bands at 3370 $cm^{-1}$ are attributed to the N–H stretching vibration of $NH_2$ group, and the bands around 1655 and 1588 $cm^{-1}$ are assigned to amide I (C]O) and amide II (N–H) [7], respectively. The bands at 1155, 1069, and 1029 $cm^{-1}$ are assigned to the C–O stretching vibrations of C–*O*–C linkage [6]. With the increase of the content of HAp, the characteristic peaks of CS weaken gradually.

### 3.3. Porosity and swelling ratio of the scaffolds

The porosity of the scaffold plays an important role in bone formation, and high porosity is usually beneficial for cell ingrowth and survival. The porosity of the CS and HAp/CS scaffolds were measured by the liquid replacement method, as shown in Fig. 3(a). The porosity of pure CS, 1% HAp/CS, 2% HAp/CS, 3% HAp/CS and 4% HAp/CS scaffolds is 85.4%, 86.9%, 88.6%, 89.8%, and 91.3%, respectively. Although the concentration of HAp has little effect on the porosity of the scaffold. It can be seen that the porosity of the scaffold slightly increases with the increase of HAp content. The porosity of the 4% HAp/CS composite scaffold is as high as above 90%.

When the scaffolds are implanted into a bone defect location, they can absorb cell growth nutrients from the body fluids and swell. Therefore, the swelling property is a key feature of the scaffolds, which can affect the shape, mechanical stability, and the efficiency of substance metabolism of the scaffolds [6,41]. The swelling behavior of different scaffolds was examined by soaking them in PBS for 24, 48, and 72 h, respectively. Fig. 3(b) shows the swelling ratio of different scaffolds. Overall, each of scaffolds displays good swelling property, which can be attributed to their hydrophilicity and microporous structure. Compared with the pure CS, all the HAp/CS composite scaffolds show decreased swelling ratio. The higher the content of HAp, the lower the swelling ratio of the scaffold. In addition, the swelling of all the scaffolds reached equilibrium after incubation in PBS for about 24 h.

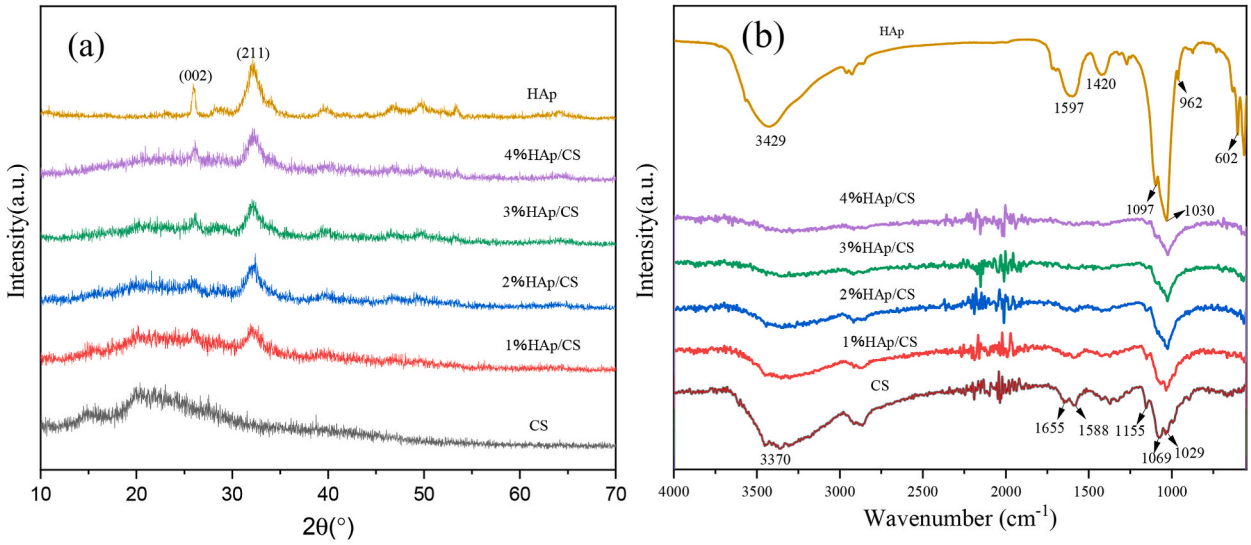


**Fig. 2.** (a) XRD patterns and (b) FTIR spectra of the HAp/CS composite scaffolds with different contents of HAp.

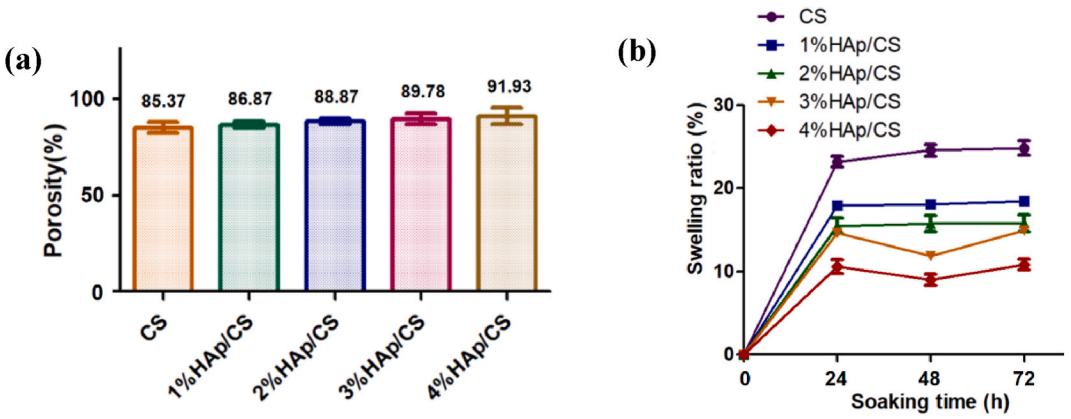


**Fig. 3.** (a) Porosity and (b) swelling ratio of the different scaffolds.

### 3.4. Mechanical properties of the scaffolds

The mechanical properties of the different scaffolds in wet state were first tested by a self-made compression experiment, as shown in Supplementary Fig. S2. It can be seen from the compressed photos that the pure CS, 1% HAp/CS, and 4% HAp/CS scaffolds exhibited obvious deformation, indicating a weak compression strength. For 4% HAp/CS scaffold, both the height and shape change a lot and the scaffold becomes fragile, which is due to the brittleness of the high inorganic content. While the 2% HAp/CS and 3% HAp/CS scaffolds maintain their height and shape integrity after compression. Fig. 4(a) and (b) shows the stress-strain curves and elastic modulus of different scaffolds, respectively. It is observed that the compressive modulus of scaffolds is significantly increased with the addition of HAp. The modulus of 3% HAp/CS scaffold (75.75 kPa) is more than twice higher than that of the pure CS scaffold (37.47 kPa), indicating the reinforcement of HAp microspheres to the CS matrix. The shape and height of the compressed samples can be recovered after soaking in PBS for a short time (insets in Fig. 4(a)), indicating a good elasticity. It is reported that there will be chemical interactions among amino groups of CS with $Ca^{2+}$ and $PO_4^{3-}$ of HAp [42,43]. These interactions provide cross-linking chains among CS and HAp, and thus results in increased mechanical properties of the HAp/CS. The more HAp is added, the more cross-linking chains are formed, and the higher the compressive strength of the composite scaffold. However, when the amount of the addition of HAp is too high, it cannot be uniformly dispersed in CS due to the aggregation, which leads to a decrease in the compressive strength of the scaffold. In this study, the 3% HAp/CS scaffold has the highest compressive modulus among all the samples. Considering the porosity, swelling ratio and mechanical properties of the scaffolds, 3% HAp/CS composite scaffolds were chosen as the research object in the following studies.

### 3.5. In vitro biocompatibility and differentiation study

An excellent biocompatibility is essential for the scaffolds used in bone regeneration [41,44]. MC3T3-E1 cell was chosen in this study for the in vitro biocompatibility of the pure CS scaffold and 3% HAp/CS composite scaffold. Fig. 5(a) and (b) shows the

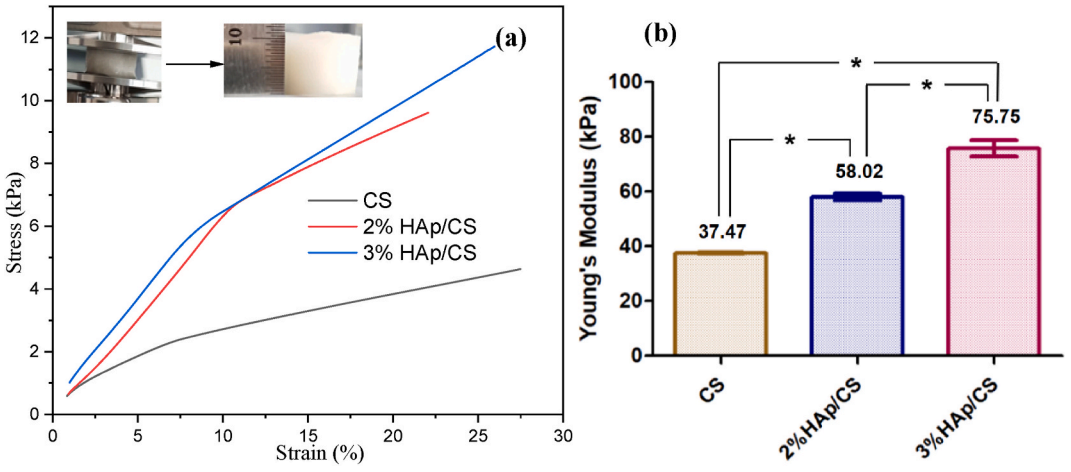


**Fig. 4.** (a) Stress-strain curves and (b) Young's modulus of different samples. (*P < 0.05).

morphology of cells after culturing for 12 days on the surface of the scaffolds. It can be observed that MC3T3-E1 cells attach and spread well with obvious pseudopod and interstitial filament formation on the surface of pure CS scaffold as well as 3% HAp/CS composite scaffold. Moreover, the cells on the 3% HAp/CS composite scaffold show more filopodia and lamellipodia formation, and can migrate and grow between the pores. The results indicated that the HAp microspheres in the CS matrix were beneficial for cell attachment and growth. This may be attributed to the uniform distribution of HAp microspheres with excellent biocompatibility and appropriate mechanical property of the composite scaffold, which provides more adhesion sites for cells, allowing for the extension of pseudopods.

ALP is considered to be an early indicator of osteogenic differentiation, and the ALP activity increases as the osteoblast differentiation develops [41,45]. We measured the ALP activity of MC3T3-E1 cells cultured with pure CS scaffold and 3% HAp/CS composite scaffold for 3, 7, and 14 days. As shown in Fig. 5(c), both CS scaffold and HAp/CS scaffold show increased ALP activity with the increasing of culture time. Moreover, the ALP activity of cells at day 14 in HAp/CS scaffold is remarkably higher than that in pure CS scaffold. The result indicates that HAp uniformly attached to the CS porous structure can effectively promote the osteogenic differentiation of MC3T3-E1 cells.

### 3.6. Bone regeneration of the scaffold in vivo

#### 3.6.1. Micro-CT evaluation

In order to evaluate the amount and quality of the newly formed bone, the Micro-CT scanning was conducted at 2, 4, and 8 weeks after surgery. It can be seen from Fig. 6(A) that there is no obvious difference of bone healing between rats treated with CS, 3% HAp/CS, and 3% HAp/CS + Periostin scaffolds at 4 weeks after implantation. However, 8 weeks after implantation, the area of the newly formed bone in 3% HAp/CS and 3% HAp/CS + Periostin groups is much larger than in CS and control groups. The uniform and continuous new bone almost completely heals the bone defect in 3% HAp/CS + Periostin group. Further, statistical analysis in Fig. 6(B) also indicated that the 3% HAp/CS + Periostin group has the highest value of BV/TV, followed by 3% HAp/CS group. The order of bone regeneration capacity for the scaffolds is 3% HAp/CS + Periostin > 3% HAp/CS > CS. These results demonstrate that periostin increases the amount of bone regeneration.

#### 3.6.2. Histological analysis

To further evaluate the efficacy of periostin for bone regeneration, the H&E staining was conducted, as shown in Fig. 7. After 2 weeks implantation, there are scattered osteoblasts in the control group and a large number of inflammatory cells and osteoblasts in CS group. A large number of osteoblasts and a small number of inflammatory cells can be observed in the 3%HAp/CS group, with scattered bone trabeculae and bone matrix present in the pores of the scaffold. In the 3%HAp/CS + Periostin group, there are abundant osteoblasts, few inflammatory cells, and irregular light pink bone trabeculae and matrix present in the gaps. With the extension of implantation time, the scaffold materials are degraded gradually and the pores of the materials have been extended. The newly formed bone trabeculae and osteogenic matrix gradually replace the scaffold material. In the 3%HAp/CS + Periostin group after 8 weeks implantation, the arrangement of bone trabeculae is regular and tight, gradually calcified into mature bone tissue, and small blood vessels appear in the mature bone.

Fig. 8 shows the Masson staining results of different groups. It can be seen that after 2 weeks implantation, blue collagen fibers are sparse and loosely arranged in the gaps, inflammatory cells are densely arranged, and the bone scaffold materials are stained dark red. After 4 weeks implantation, the number of the newly formed collagen fibers in the control and CS groups increases compared to 2 W. The newly formed collagen fibers in the 3% HAp/CS group are not significantly different from those at 2 W, while those in the 3%HAp/CS + Periostin group increase significantly. The collagen fibers are connected to each other and form a collagen fiber network. After 8 weeks implantation, the collagen fiber network in the 3%HAp/CS + Periostin group is thickened and arranged in a sheet-like manner, with cartilage present on a small amount of mature collagen fibers.

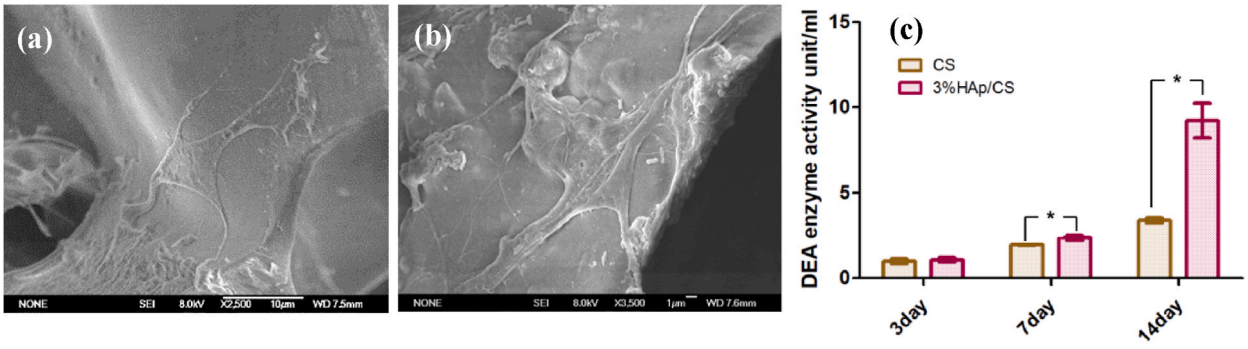


**Fig. 5.** FESEM images of MC3T3-E1 cells cultured on (a) pure CS scaffold and (b) HAp/CS composite scaffold for 12 days. (c) ALP activity of MC3T3-E1 cells cultured on different samples. (*P < 0.05).

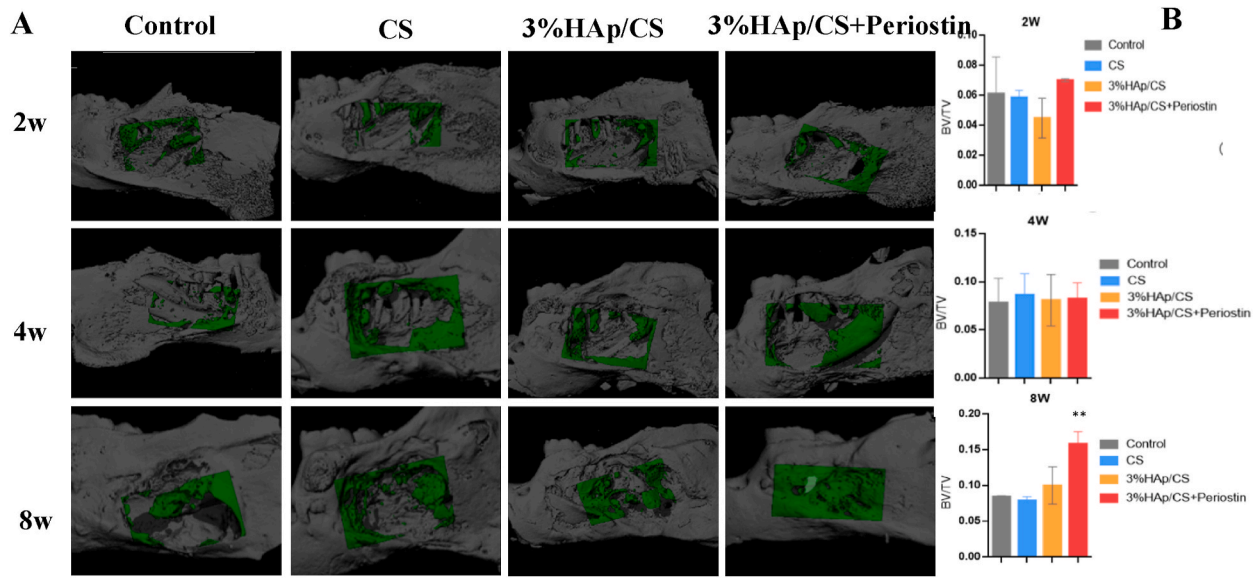


**Fig. 6.** Bone healing ability of different groups. (A) 3D reconstructed Micro-CT images of bone regeneration of the bone defects after implantation. (B) Quantitative comparison of BV/TV among different groups.

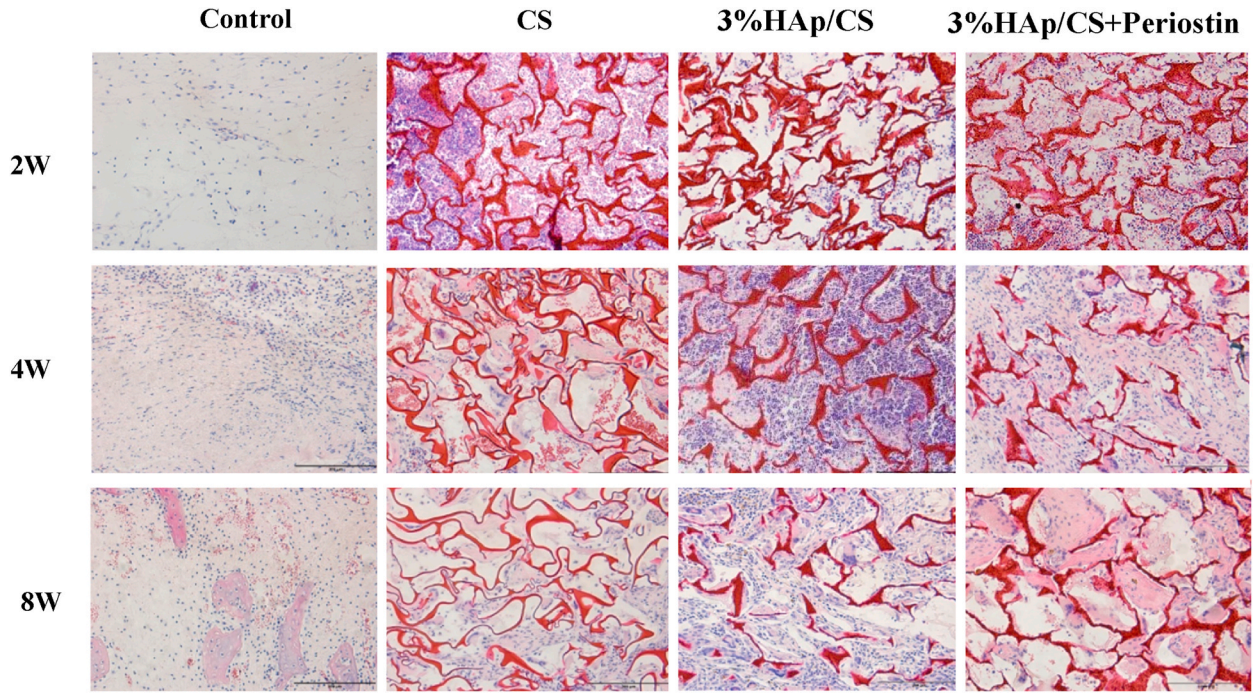


**Fig. 7.** Histological sections of the bone regeneration after H&E staining.

### *3.6.3. Immunohistochemical and TRAP staining analysis*

To further investigate osteogenesis within the porous scaffolds, cross sections in the middle of the bone defects were submitted for immunohistochemical evaluation, as shown in Fig. 9(A). It can be seen from Fig. 9(B) that the ALP activity in the 3%HAp/CS + Periostin group is the highest among all the groups. For the expression of Col I, the 3%HAp/CS group is obviously higher than the CS group, while the 3%HAp/CS + Periostin group shows the highest expression. Col I is considered as the basic initial bone matrix protein in bone formation, the higher amount of Col I in 3%HAp/CS + Periostin group would be beneficial for cell attachment and migration in tissues and subsequent skeletal reconstruction [46]. OCN is synthesized only by mature osteoblasts during mineralization [47]. Similarly, the 3%HAp/CS + Periostin group shows a remarkably higher OCN expression in comparison to other groups, which

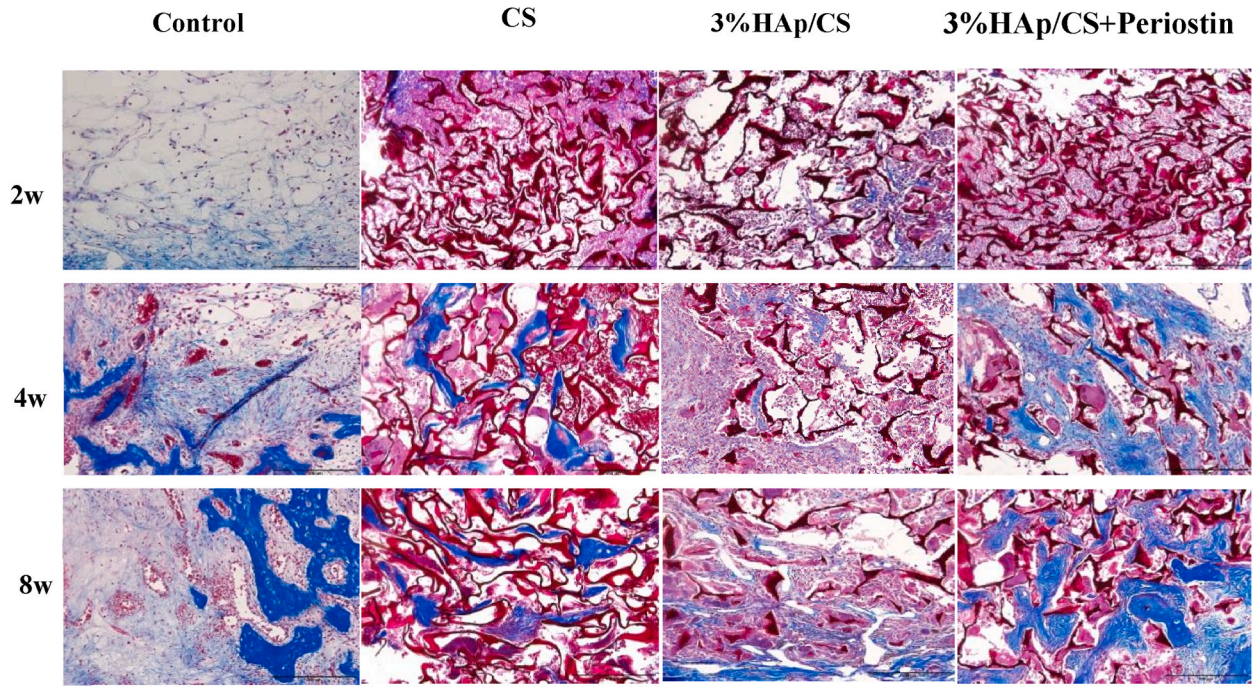


**Fig. 8.** Histological sections of the bone regeneration after Masson staining.

indicates that the loaded periostin in scaffold accelerates matrix mineralization. TRAP is a specific marker enzyme for osteoclasts. It can be seen from Fig. 9(A) that the control, CS, and 3%HAp/CS groups exhibit multiple TRAP positive osteoclasts at the defect sites. However, very few osteoclasts are present in the 3%HAp/CS + Periostin group.

## 4. Conclusions

In summary, the hollow HAp microspheres with an urchin-like microstructure and high surface area were firstly prepared by a hydrothermal method. Then, the HAp/CS composite scaffolds were fabricated through using a simple freeze-drying method without using any chemical cross-linkers. The HAp/CS composite scaffolds exhibited interconnected pores with large pore size and high porosity. When the content of HAp microspheres reached 3%, the HAp/CS composite scaffolds showed improved compressive elastic modulus. The addition of HAp microspheres into CS matrix can effectively enhance the cell adhesion and stimulate the osteogenic differentiation of cells. Moreover, periostin can be loaded onto the HAp/CS scaffold and released during bone repair. In vivo experiment results demonstrated that the HAp/CS scaffold loaded with periostin can inhibit osteoclastic bone resorption and promote osteoblast proliferation, as well as enhance osteointegration and accelerate bone regeneration. Therefore, the as-prepared HAp/CS composite scaffold loaded with periostin would potentially be a promising material for bone filling and regeneration.

## Ethics approval

This study complied with all ethical norms, and the study involving rats was approved by the Ethics Committee of Shandong University Stomatological Hospital for animal experimental ethics review. (ethics approval number: 20220906).

## Data availability statement

Data will be made available on request and no data was stored in any publicly available repository.

## CRediT authorship contribution statement

**Huachun Wang:** Writing – original draft, Methodology, Investigation, Data curation, Conceptualization. **Ruixue Sun:** Writing – review & editing, Conceptualization. **Shengyun Huang:** Writing – review & editing, Data curation. **Haiwei Wu:** Validation, Data curation. **Dongsheng Zhang:** Writing – review & editing, Supervision.

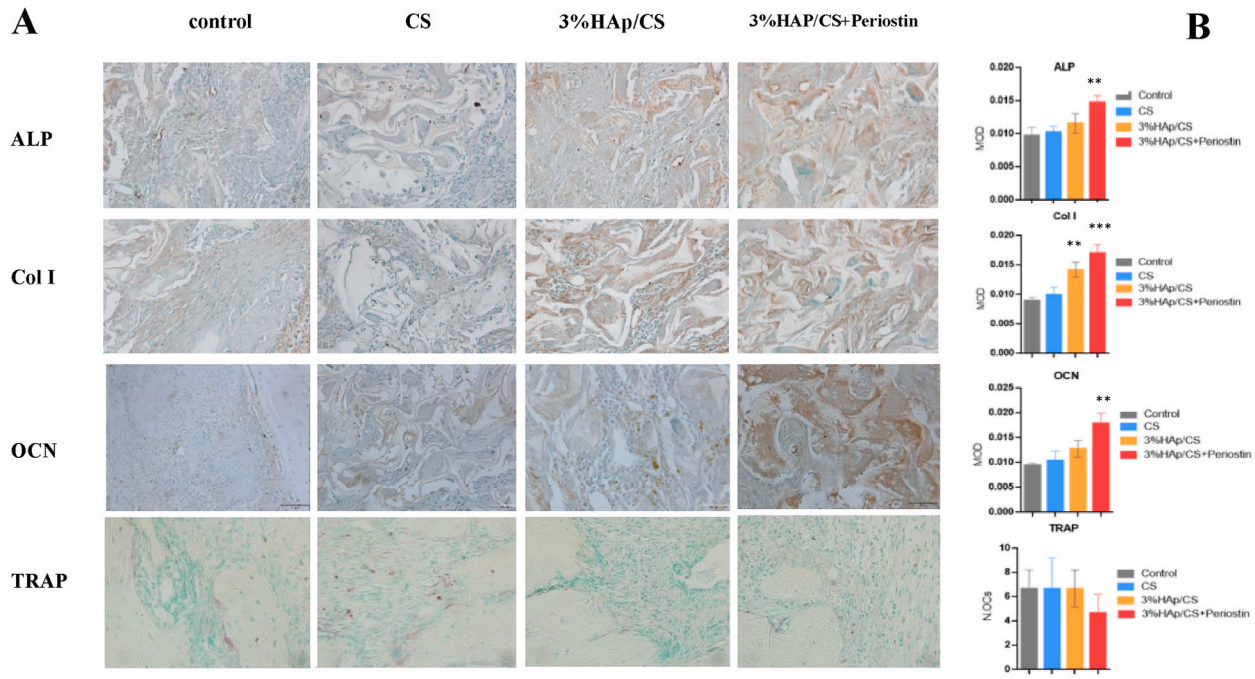


**Fig. 9.** (A) Representative immunohistochemical staining and (B) Quantitative comparison of the bone defects from each group after 8 weeks implantation.

## Declaration of competing interest

The authors declare that they have no known competing financial interests or personal relationships that could have appeared to influence the work reported in this paper.

## Appendix A. Supplementary data

Supplementary data to this article can be found online at https://doi.org/10.1016/j.heliyon.2024.e25832.

## References

[1] S.K.L. Levengood, M. Zhang, Chitosan-based scaffolds for bone tissue engineering, J. Mater. Chem. B 2 (21) (2014) 3161–3184.
[2] T.-T. Li, Y. Zhang, H.-T. Ren, H.-K. Peng, C.-W. Lou, J.-H. Lin, Two-step strategy for constructing hierarchical pore structured chitosan–hydroxyapatite composite scaffolds for bone tissue engineering, Carbohydr. Polym. 260 (2021) 117765.
[3] J. Wen, J. Liao, Q. Ying, H. Li, Y. Mao, S. Han, Y. Zhu, Improvement of in vitro degradation of magnesium oxychloride cement for bone repair by chitosan, J. Mater. Sci. 56 (1) (2020) 706–717.
[4] X. Zhang, Y. Zhang, G. Ma, D. Yang, J. Nie, The effect of the prefrozen process on properties of a chitosan/hydroxyapatite/poly(methyl methacrylate) composite prepared by freeze drying method used for bone tissue engineering, RSC Adv. 5 (97) (2015) 79679–79686.
[5] C. Dai, Y. Li, W. Pan, G. Wang, R. Huang, Y. Bu, X. Liao, K. Guo, F. Gao, Three-dimensional high-porosity chitosan/honeycomb porous carbon/hydroxyapatite scaffold with enhanced osteoinductivity for bone regeneration, ACS Biomater. Sci. Eng. 6 (1) (2020) 575–586.
[6] N.K. Nga, L.T. Thanh Tam, N.T. Ha, P. Hung Viet, T.Q. Huy, Enhanced biomineralization and protein adsorption capacity of 3D chitosan/hydroxyapatite biomimetic scaffolds applied for bone-tissue engineering, RSC Adv. 10 (70) (2020) 43045–43057.
[7] X. Cai, L. Chen, T. Jiang, X. Shen, J. Hu, H. Tong, Facile synthesis of anisotropic porous chitosan/hydroxyapatite scaffolds for bone tissue engineering, J. Mater. Chem. 21 (32) (2011) 12015.
[8] M. Demirel, A.I. Kaya, Effect of strontium-containing compounds on bone grafts, J. Mater. Sci. 55 (15) (2020) 6305–6329.
[9] H. Li, C. Hu, H. Yu, C. Chen, Chitosan composite scaffolds for articular cartilage defect repair: a review, RSC Adv. 8 (7) (2018) 3736–3749.
[10] P. Sahariah, M. Másson, Antimicrobial chitosan and chitosan derivatives: a review of the structure–activity relationship, Biomacromolecules 18 (11) (2017) 3846–3868.
[11] C.Y. Goh, S.S. Lim, K.Y. Tshai, A.W.Z.Z. El Azab, H.-S. Loh, Fabrication and in vitro biocompatibility of sodium tripolyphosphate-crosslinked chitosan–hydroxyapatite scaffolds for bone regeneration, J. Mater. Sci. 54 (4) (2018) 3403–3420.
[12] P. Chen, L. Liu, J. Pan, J. Mei, C. Li, Y. Zheng, Biomimetic composite scaffold of hydroxyapatite/gelatin-chitosan core-shell nanofibers for bone tissue engineering, Mater. Sci. Eng. C 97 (2019) 325–335.
[13] B.H. Atak, B. Buyuk, M. Huysal, S. Isik, M. Senel, W. Metzger, G. Cetin, Preparation and characterization of amine functional nano-hydroxyapatite/chitosan bionanocomposite for bone tissue engineering applications, Carbohydr. Polym. 164 (2017) 200–213.
[14] N. Bhardwaj, S.C. Kundu, Chondrogenic differentiation of rat MSCs on porous scaffolds of silk fibroin/chitosan blends, Biomaterials 33 (10) (2012) 2848–2857.

[15] A. Ressler, J. Ródenas-Rochina, M. Ivanković, H. Ivanković, A. Rogina, G. Gallego Ferrer, Injectable chitosan-hydroxyapatite hydrogels promote the osteogenic differentiation of mesenchymal stem cells, Carbohydr. Polym. 197 (2018) 469–477.
[16] C. Koski, A.A. Vu, S. Bose, Effects of chitosan-loaded hydroxyapatite on osteoblasts and osteosarcoma for chemopreventative applications, Mater. Sci. Eng. C 115 (2020) 111041.
[17] X. Xie, Y. Xiao, K. Xu, Z. Xu, Design of Sr-doped hydroxyapatite nanoparticles loaded on chitosan scaffold for promoting the spinal cord injury repair, Mater. Lett. 267 (2020) 127471.
[18] M.K. Ahmed, S.F. Mansour, R. Al-Wafi, S.I. El-dek, V. Uskoković, Tuning the mechanical, microstructural, and cell adhesion properties of electrospun ε-polycaprolactone microfibers by doping selenium-containing carbonated hydroxyapatite as a reinforcing agent with magnesium ions, J. Mater. Sci. 54 (23) (2019) 14524–14544.
[19] J.P. Monte, A. Fontes, B.S. Santos, G.A.L. Pereira, G. Pereira, Recent advances in hydroxyapatite/polymer/silver nanoparticles scaffolds with antimicrobial activity for bone regeneration, Mater. Lett. 338 (2023) 134027.
[20] H. He, L. Wang, X. Cai, Q. Wang, P. Liu, J. Xiao, Biomimetic collagen composite matrix-hydroxyapatite scaffold induce bone regeneration in critical size cranial defects, Mater. Des. 236 (2023) 112510.
[21] S.F. Mansour, S.I. El-dek, S.V. Dorozhkin, M.K. Ahmed, Physico-mechanical properties of Mg and Ag doped hydroxyapatite/chitosan biocomposites, New J. Chem. 41 (22) (2017) 13773–13783.
[22] L. Gritsch, M. Maqbool, V. Mouriño, F.E. Ciraldo, M. Cresswell, P.R. Jackson, C. Lovell, A.R. Boccaccini, Chitosan/hydroxyapatite composite bone tissue engineering scaffolds with dual and decoupled therapeutic ion delivery: copper and strontium, J. Mater. Chem. B 7 (40) (2019) 6109–6124.
[23] A. Rogina, M. Ivanković, H. Ivanković, Preparation and characterization of nano-hydroxyapatite within chitosan matrix, Mater. Sci. Eng. C 33 (8) (2013) 4539–4544.
[24] B. Gaihre, S. Uswatta, A.C. Jayasuriya, Nano-scale characterization of nano-hydroxyapatite incorporated chitosan particles for bone repair, Colloids Surf., B 165 (2018) 158–164.
[25] Y. Zhang, J.R. Venugopal, A. El-Turki, S. Ramakrishna, B. Su, C.T. Lim, Electrospun biomimetic nanocomposite nanofibers of hydroxyapatite/chitosan for bone tissue engineering, Biomaterials 29 (32) (2008) 4314–4322.
[26] X.-q. Liu, X.-x. Zhao, Y. Liu, T.-a. Zhang, Review on preparation and adsorption properties of chitosan and chitosan composites, Polym. Bull. 79 (4) (2021) 2633–2665.
[27] M.A. Nazeer, E. Yilgör, I. Yilgör, Intercalated chitosan/hydroxyapatite nanocomposites: promising materials for bone tissue engineering applications, Carbohydr. Polym. 175 (2017) 38–46.
[28] T.W. Sun, Y.J. Zhu, F. Chen, Highly flexible multifunctional biopaper comprising chitosan reinforced by ultralong hydroxyapatite nanowires, Chem. Eur J. 23 (16) (2017) 3850–3862.
[29] N. Nezafati, R. Faridi-Majidi, M. Pazouki, S. Hesaraki, Synthesis and characterization of a novel freeze-dried silanated chitosan bone tissue engineering scaffold reinforced with electrospun hydroxyapatite nanofiber, Polym. Int. 68 (8) (2019) 1420–1429.
[30] X. Wei, Q. Liu, L. Liu, W. Tian, Y. Wu, S. Guo, Periostin plays a key role in maintaining the osteogenic abilities of dental follicle stem cells in the inflammatory microenvironment, Arch. Oral Biol. 153 (2023) 105737.
[31] J. Cai, H. Qin, G. Yu, Effect of periostin silencing on Runx2, RANKL and OPG expression in osteoblasts, J. Orofac. Orthop. 82 (2) (2020) 82–91.
[32] Q. Zhao, D. Zhang, R. Sun, S. Shang, H. Wang, Y. Yang, L. Wang, X. Liu, T. Sun, K. Chen, Adsorption behavior of drugs on hydroxyapatite with different morphologies: a combined experimental and molecular dynamics simulation study, Ceram. Int. 45 (15) (2019) 19522–19527.
[33] X. Jiang, D. Zhang, R. Sun, H. Wang, Y. Yang, H. Guo, Y. Tang, A combined experimental and molecular dynamics simulation study on doxorubicin adsorption on strontium-substituted hydroxyapatite hollow microspheres, Appl. Surf. Sci. 542 (2021) 148667.
[34] R. Das, S. Karthika, J. Bhasarkar, D.K. Bal, GA-coupled ANN model for predicting porosity in alginate gel scaffolds, J. Mech. Behav. Biomed. Mater. 148 (2023) 106204.
[35] Y.S. Pereira, F.S. Lameiras, A.M.M. dos Santos, Geopolymer foam reinforced with iron ore flotation tailing for potassium adsorption and controlled release in water, ACS Omega 8 (48) (2023) 45735–45749.
[36] N. Abdian, M. Etminanfar, S.O.R. Sheykholeslami, H. Hamishehkar, J. Khalil-Allafi, Preparation and characterization of chitosan/hydroxyapatite scaffolds containing mesoporous SiO2-HA for drug delivery applications, Mater. Chem. Phys. 301 (2023) 127672.
[37] P. Ma, W. Wu, Y. Wei, L. Ren, S. Lin, J. Wu, Biomimetic gelatin/chitosan/polyvinyl alcohol/nano-hydroxyapatite scaffolds for bone tissue engineering, Mater. Des. 207 (2021) 109865.
[38] B. Kaczmarek, A. Sionkowska, A.M. Osyczka, Physicochemical properties of scaffolds based on mixtures of chitosan, collagen and glycosaminoglycans with nano-hydroxyapatite addition, Int. J. Biol. Macromol. 118 (2018) 1880–1883.
[39] G. Wang, L. Zheng, H. Zhao, J. Miao, C. Sun, H. Liu, Z. Huang, X. Yu, J. Wang, X. Tao, Construction of A Fluorescent nanostructured chitosan-hydroxyapatite scaffold by nanocrystallon induced biomimetic mineralization and its cell biocompatibility, ACS Appl. Mater. Interfaces 3 (5) (2011) 1692–1701.
[40] M. Sumathra, K.K. Sadasivuni, S.S. Kumar, M. Rajan, Cisplatin-loaded graphene oxide/chitosan/hydroxyapatite composite as a promising tool for osteosarcoma-affected bone regeneration, ACS Omega 3 (11) (2018) 14620–14633.
[41] X. Ding, X. Li, C. Li, M. Qi, Z. Zhang, X. Sun, L. Wang, Y. Zhou, Chitosan/dextran hydrogel constructs containing strontium-doped hydroxyapatite with enhanced osteogenic potential in rat cranium, ACS Biomater. Sci. Eng. 5 (9) (2019) 4574–4586.
[42] A. Zima, Hydroxyapatite-chitosan based bioactive hybrid biomaterials with improved mechanical strength, Spectrochim. Acta Mol. Biomol. Spectrosc. 193 (2018) 175–184.
[43] C. Sharma, A.K. Dinda, P.D. Potdar, C.-F. Chou, N.C. Mishra, Fabrication and characterization of novel nano-biocomposite scaffold of chitosan–gelatin–alginate–hydroxyapatite for bone tissue engineering, Mater. Sci. Eng. C 64 (2016) 416–427.
[44] M. Swetha, K. Sahithi, A. Moorthi, N. Srinivasan, K. Ramasamy, N. Selvamurugan, Biocomposites containing natural polymers and hydroxyapatite for bone tissue engineering, Int. J. Biol. Macromol. 47 (1) (2010) 1–4.
[45] S. Li, X. Pu, X. Chen, X. Liao, Z. Huang, G. Yin, A novel bi-phase Sr-doped magnesium phosphate/calcium silicate composite scaffold and its osteogenesis promoting effect, Ceram. Int. 44 (14) (2018) 16237–16245.
[46] H. Quan, Y. He, J. Sun, W. Yang, W. Luo, C. Dou, F. Kang, C. Zhao, J. He, X. Yang, S. Dong, H. Jiang, Chemical self-assembly of multifunctional hydroxyapatite with a coral-like nanostructure for osteoporotic bone reconstruction, ACS Appl. Mater. Interfaces 10 (30) (2018) 25547–25560.
[47] L. Wang, Y. Qiu, Y. Guo, Y. Si, L. Liu, J. Cao, J. Yu, X. Li, Q. Zhang, B. Ding, Smart, elastic, and nanofiber-based 3D scaffolds with self-deploying capability for osteoporotic bone regeneration, Nano Lett. 19 (12) (2019) 9112–9120.